

Constraining Scatter in the Stellar Mass–Halo Mass Relation for Haloes Less Massive than the Milky Way

Magdalena Allen,¹ Peter Behroozi,² and Chung-Pei Ma^{1,3}

¹*Department of Astronomy, University of California, Berkeley, CA 94720, USA*

²*Department of Astronomy and Steward Observatory, University of Arizona, Tucson, AZ 85721, USA*

³*Department of Physics, University of California, Berkeley, CA 94720, USA*

17 December 2018

ABSTRACT

Most galaxies are hosted by massive, invisible dark matter haloes, yet little is known about the scatter in the stellar mass–halo mass relation for galaxies with host halo masses $M_h \leq 10^{11} M_\odot$. Using mock catalogs based on dark matter simulations, we find that two observable signatures are sensitive to scatter in the stellar mass–halo mass relation even at these mass scales; i.e., conditional stellar mass functions and velocity distribution functions for neighbouring galaxies. We compute these observables for 179,373 galaxies in the Sloan Digital Sky Survey (SDSS) with stellar masses $M_* > 10^9 M_\odot$ and redshifts $0.01 < z < 0.307$. We then compare to mock observations generated from the *Bolshoi-Planck* dark matter simulation for stellar mass–halo mass scatters ranging from 0 to 0.6 dex. The observed results are consistent with simulated results for low values of scatter (~ 0.2 dex), but SDSS statistics are insufficient to provide firm constraints. This method could provide much tighter constraints on stellar mass–halo mass scatter in the future if applied to larger data sets, especially the anticipated Dark Energy Spectroscopic Instrument Bright Galaxy Survey, and constraining the scatter could have important implications for galaxy formation and evolution.

Key words: galaxies: haloes – galaxies: statistics – galaxies: formation – galaxies: evolution

1 INTRODUCTION

In the Λ CDM paradigm, galaxies grow at the centres of virialized, self-bound dark matter haloes. Halo formation is hierarchical, such that smaller self-bound *satellite* haloes can be found within the virial radii of larger haloes; haloes that are not contained within a larger virialized structure are known as *central* haloes.

While galaxy stellar mass correlates with halo mass, this correlation is not perfect. At halo masses $M_h > 10^{12} M_\odot$, there are multiple ways to estimate scatter in the galaxy–halo connection, including galaxy clustering, group catalogs, direct X-ray masses, and satellite kinematics. These methods have converged on 0.15 – 0.23 dex of stellar mass scatter for such haloes, with no apparent dependence on halo mass (More et al. 2009; Reddick et al. 2013; Tinker et al. 2017; Kravtsov et al. 2018).

Considerably less is known about the stellar mass scatter for lower-mass haloes. The shape of the stellar mass–halo mass relation results in galaxy formation becoming rapidly more inefficient for haloes with masses lower than $M_h \sim 10^{12} M_\odot$ (Moster et al. 2010, 2013; Behroozi et al. 2010, 2013c; Garrison-Kimmel et al. 2014). Thus, low-mass galaxies have fewer satellites (limiting group catalog and satellite

kinematics approaches), no mass-dependence in their bias (Tinker et al. 2010, limiting clustering techniques), and their surrounding gas is too cold to emit detectable levels of X-rays.

At the same time, there has been increased interest in the stellar mass–halo mass scatter for $M_h < 10^{12} M_\odot$ due to the “too big to fail” problem (Boylan-Kolchin et al. 2011), wherein dark matter-only simulations overpredict the numbers of dense satellites. One way to resolve this problem is for low-mass ($M_h \lesssim 3 \times 10^9 M_\odot$) satellites to have large amounts of scatter in stellar mass at fixed halo mass, which is indeed a generic prediction from hydrodynamical simulations (Sawala et al. 2016; Munshi et al. 2017). If, on the other hand, the scatter remains tight, then several authors have proposed that warm or self-interacting dark matter models are necessary to resolve the problem (Boylan-Kolchin et al. 2011; Elbert et al. 2015; Garrison-Kimmel et al. 2017; Garcia-Cely & Chu 2017).

Here, we describe a method to measure scatter in lower-mass haloes that is based on forward modeling. Briefly, we use abundance matching (Nagai & Kravtsov 2005; Conroy et al. 2006; Behroozi et al. 2010; Moster et al. 2010; Reddick et al. 2013) to populate haloes with galaxies in a dark

arXiv:1812.05733v1 [astro-ph.GA] 13 Dec 2018

matter simulation with different amounts of scatter. In this technique, galaxies in a given observed volume are assigned by rank order in mass to dark matter haloes (also rank ordered by mass) in an equivalent simulated volume; these assignments are then perturbed iteratively until the desired scatter is achieved. We show that velocity distribution functions and conditional stellar mass functions are both sensitive to the level of stellar mass–halo mass scatter. Intuitively, larger scatters allow lower-mass haloes to host larger galaxies, hence reducing satellite counts in conditional stellar mass functions. At the same time, smaller galaxies can be hosted by larger-mass haloes, thus broadening velocity distributions.

The use of two different scatter-sensitive techniques is important, as a key uncertainty is when satellite haloes (i.e., haloes within the virial radius of a larger halo) are considered merged. Generally, higher-resolution simulations track satellite haloes longer (Onions et al. 2012), and so would give higher predictions for conditional stellar mass functions *and* velocity distribution functions at fixed scatter. The same is true if satellites are tracked after disappearance using “orphan” techniques (e.g., Kitzbichler & White 2008). Hence, using two different techniques allows for self-consistently breaking this degeneracy.

We present the observational and simulated data sets in §2, our method for calculating velocity distribution functions and conditional stellar mass functions in §3, results and discussion in §4, and conclusions in §5. The analysis here adopts a flat, Λ CDM cosmology ($\Omega_M = 0.307$, $\Omega_\Lambda = 0.693$, $h = 0.678$, $n_s = 0.96$, $\sigma_8 = 0.823$) consistent with the *Planck* 2015 results (Ade et al. 2016). Stellar masses assume a Chabrier (2003) initial mass function, and halo masses use the virial spherical overdensity definition from Bryan & Norman (1998).

2 DATA

2.1 Observations

Here, we describe the selection of 179,373 Sloan Digital Sky Survey target galaxies with $M_* > 10^9 M_\odot$ and $0.01 < z < 0.307$ (§2.1.1), the corrections applied (§2.1.2), and the method of error calculation (§2.1.3).

2.1.1 Catalogs

Redshifts are taken from the Sloan Digital Sky Survey (SDSS) Release 10 (Ahn et al. 2014), and have over 90% completeness for galaxies brighter than the SDSS r-band apparent magnitude limit of 17.77. As determined in §3 of Behroozi et al. (2015), this corresponds to a stellar mass completeness limit as a function of redshift given by:

$$17.77 = r < -0.25 - 1.9 \log_{10} \left(\frac{M_*}{M_\odot} \right) + 5 \log_{10} \left(\frac{D_L(z)}{10 \text{ pc}} \right) \quad (1)$$

where M_* is the stellar mass and $D_L(z)$ is the luminosity distance for our assumed cosmology. Median total stellar masses and star formation rates (SFRs) are from the MPA-JHU value-added catalog (Kauffmann et al. 2003; Brinchmann et al. 2004), updated for the imaging and spectroscopy in the SDSS Data Release 7 (Abazajian et al. 2009) and

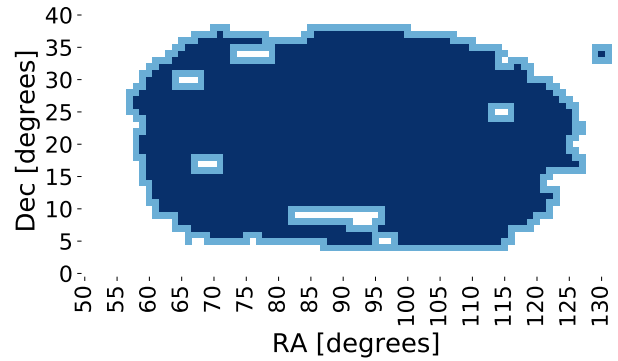


Figure 1. Map showing SDSS survey regions included (dark blue) and excluded (light blue) for this analysis.

both calculated assuming Chabrier (2003) initial mass functions (IMFs). All galaxy targets are taken with $z > 0.01$ to minimize the effect of peculiar velocities on their inferred distances.

As described in §3.1, we use isolation criteria to preferentially select central galaxies for this analysis. The fraction of isolated galaxies was found to vary significantly in regions close to survey boundaries. Hence, we excluded galaxies within any bin (2 degrees in right ascension by 2 degrees declination) bordering survey edges (Figure 1) from our isolated samples, but allowed such galaxies to be included in total neighbour counts. The final cut included 179,373 targets with $M_* > 10^9 M_\odot$ over 5706 square degrees of sky, with a maximum observed redshift of 0.307.

2.1.2 Galaxy Weights

Close galaxy pairs (separated by less than 55 arcseconds) are under-selected in the SDSS due to fibre collisions, so we apply a statistical weight w_C to each galaxy in close pairs to compensate. This correction is first estimated as a function of angular separation, based on a functional model of the incompleteness of spectroscopic pairs compared to photometric pairs as defined in Patton et al. 2002, §5.3. We take w_C to be 3.08, as calculated for a similar SDSS sample in Patton et al. 2013, §3.

Due to the SDSS magnitude limit given in Equation 1, a galaxy of any given stellar mass is only detectable to a certain maximum redshift distance z_{max} . We therefore assign each galaxy a volume correction weight

$$w_V = 1/V(z_{max}) \quad (2)$$

where $V(z)$ is the comoving volume out to redshift z . To correct for under-selected central galaxies, we use these weights when averaging neighbour counts for the distributions detailed in §3.2 and §3.3.

However, even if a central galaxy is detected at z_1 , its neighbours may still be underrepresented, and so a different correction is made:

$$w_V = \frac{1}{\max(V_c, V_n)} \quad (3)$$

where V_c is the maximum observable volume of the central galaxy and V_n is the same for the neighbour; w_V is thus the

inverse of the maximum observable volume for the pair. The final weight applied to each galaxy is then $w_C w_V$.

2.1.3 Error Analysis

Errors on neighbour and central galaxy counts (due to sample variance) are calculated via spatial bootstrap resampling. The observed catalog is divided into regions of 10×10 degrees (in RA and Dec) and randomly resampled 100 times to produce reconstructed sky surveys within $<1\%$ of the original area. Regions of 10×10 degrees are chosen to preserve local structure and resample on scales where the Universe becomes homogeneous (>10 Mpc/h), though not much difference in error estimates is seen between using 2×2 and 10×10 degree regions in the resampling. The distributions described in §3 are then computed for the resampled catalogs and the standard deviation calculated. Our simulated catalogs are much larger in volume than our observed sample, and so we assume that the error budget is dominated by observational sample variance.

2.2 Mock Catalogs

Here, we describe the generation of simulated dark matter haloes (§2.2.1), the addition of orphan satellites (§2.2.2), and the process of assigning galaxy masses to account for variable scatter in the halo mass–stellar mass relation (§2.2.3).

2.2.1 Dark Matter Simulation

We base our mock catalogs on the *Bolshoi-Planck* dark matter simulation (Klypin et al. 2016; Rodríguez-Puebla et al. 2016). The simulation followed 2048³ particles (~ 8 billion) each of mass $1.55 \times 10^8 M_\odot/h$ in a periodic box of comoving side length 250 Mpc/h from $z = 100$ to $z = 0$, using the ART code (Kravtsov et al. 1997; Kravtsov & Klypin 1999). The adopted flat Λ CDM cosmology was consistent with *Planck* 2015 results ($\Omega_M = 0.307$, $\Omega_\Lambda = 0.693$, $h = 0.678$, $n_s = 0.96$, $\sigma_8 = 0.823$). Haloes were found using the ROCKSTAR phase-space halo finder (Behroozi et al. 2013a) and the CONSISTENT TREES merger tree code (Behroozi et al. 2013b).

2.2.2 Orphan Satellites

A significant uncertainty with simulations is how long satellite haloes persist before disruption. In large cosmological simulations, it is often necessary to include “orphan” satellites to match galaxy clustering (Kitzbichler & White 2008; Moster et al. 2018; Behroozi et al. 2018); here, we generate catalogs with orphans as they are required to best match observations.

Orphan satellite haloes were added to the *Bolshoi-Planck* halo catalogs following the prescription in Behroozi et al. (2018). Briefly, satellites that disappear in the simulation are presumed to continue orbiting their last host halo; we integrate their continued motion using a softened gravity law:

$$\dot{\mathbf{v}} = \frac{GM_{\text{host}}(< r)}{(r + 0.1R_{\text{vir,host}})^2} \quad (4)$$

where $M_{\text{host}}(< r)$ is the mass enclosed within the satellite

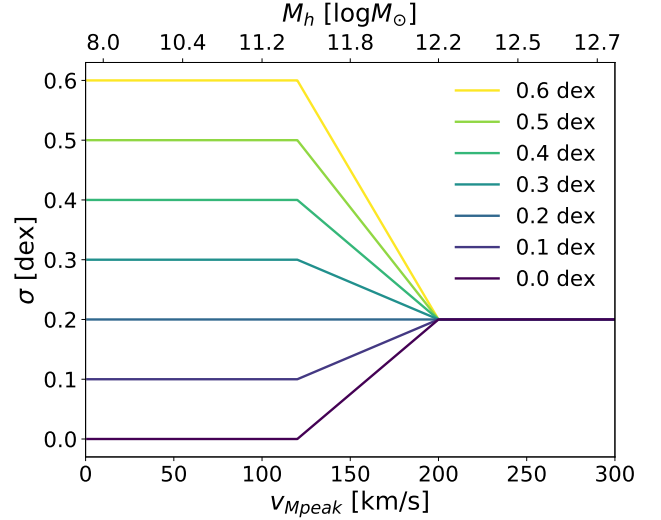


Figure 2. Functional form of scatter in dex for each tested model, as a function of the maximum circular velocity at the time the halo reached peak mass (v_{Mpeak}). The equivalent peak halo mass appears on the top axis. All models are consistent with prior observable constraints; i.e., that the scatter in stellar mass is ~ 0.2 dex for halos of mass $M_h > 10^{12} M_\odot$.

distance r , $R_{\text{vir,host}}$ is the virial radius of the host halo, and the softening is performed to avoid unphysical hard scattering between the satellite and the host halo. The choice to include orphan haloes is motivated by comparison with observations in Appendix B.

Satellite mass loss follows Jiang & van den Bosch (2016), with the modification that satellites do not lose mass on infalling orbits and lose mass at twice the rate on outgoing orbits (Behroozi et al. 2018). Satellites are assumed to disrupt once their maximum circular velocity ($v_{\text{max}} \equiv \max_R \sqrt{GM(< R)/R}$) falls below $0.6v_{\text{Mpeak}}$, where v_{Mpeak} is the maximum circular velocity at the time the halo reached peak mass. This prescription results in $\sim 25\%$ more satellites independent of mass, and was found in Behroozi et al. (2018) to give the best match to galaxy autocorrelation functions.

2.2.3 Assigning Galaxy Masses

Galaxy masses are assigned using an abundance matching approach (e.g., Marinoni & Hudson 2002; Nagai & Kravtsov 2005; Conroy et al. 2006; Reddick et al. 2013) to the dark matter halo catalog (including orphans) at $z = 0$. We compute galaxy number densities from the selected SDSS regions (included in Figure 1, totaling 5706 square degrees) using the inverse volume weights described in Eq. 2. We compute the resulting number of galaxies as a function of mass that would be expected within the simulation volume. These galaxies are ordered by decreasing mass and assigned to haloes in order of decreasing v_{Mpeak} with zero scatter. We then introduce v_{Mpeak} -dependent log-normal scatter of $\sigma(v_{\text{Mpeak}})$ via the following iterative algorithm:

(i) Each scattered mass M'_* is drawn from a log-normal distribution centered on the assigned stellar mass M_* and

of width $\sigma(v_{\text{Mpeak}})$. This introduces the correct scatter, but deforms the shape of the total stellar mass function.

(ii) Redo abundance matching (with the original SDSS galaxy number densities) to haloes ordered by decreasing M_* . This corrects the shape of the stellar mass function, but alters the distribution of the scatter.

(iii) Recompute the median $M_*(v_{\text{Mpeak}})$ relation from the stellar masses assigned in step (ii). End algorithm if median relation changes by less than 1% from previous iteration. This step approximates the change in the median $M_*(v_{\text{Mpeak}})$ relation necessary to reproduce the correct stellar mass function after adding scatter.

(iv) Assign stellar masses to halos with zero scatter according to the computed median $M_*(v_{\text{Mpeak}})$ relation and go to step (i).

This can be recognized as a simple deconvolution algorithm, as discussed further in Behroozi et al. (2010).

Because the scatter for massive haloes ($M_h > 10^{12}M_\odot$) is already constrained to be ~ 0.2 dex (Reddick et al. 2013), we adopt the following functional form for $\sigma(v_{\text{Mpeak}})$, with a given scatter X for low-mass haloes:

$$\frac{\sigma(v_{\text{Mpeak}}, X)}{\text{dex}} = \begin{cases} 0.2 & \text{if } v_{\text{Mpeak}} > 200 \text{ km s}^{-1} \\ X & \text{if } v_{\text{Mpeak}} < 120 \text{ km s}^{-1} \\ X + (0.2 - X)L(v_{\text{Mpeak}}) & \text{otherwise} \end{cases} \quad (5)$$

where $L(v_{\text{Mpeak}})$ linearly interpolates from 0 to 1 as v_{Mpeak} goes from 120 to 200 km s^{-1} :

$$L(v_{\text{Mpeak}}) = \frac{v_{\text{Mpeak}} - 120 \text{ km s}^{-1}}{200 \text{ km s}^{-1} - 120 \text{ km s}^{-1}} \quad (6)$$

This smoothly varies the scatter from 0.2 for $\sim 10^{12}M_\odot$ haloes to X for $\sim 10^{11}M_\odot$ and smaller haloes. Here, we test seven different values of X , i.e., 0.0, 0.1, 0.2, 0.3, 0.4, 0.5, and 0.6; the resulting functions for $\sigma(v_{\text{Mpeak}})$ are plotted in Fig. 2.

3 METHODS

Here, we describe methods for selecting isolated galaxies (§3.1) as well as for measuring conditional stellar mass functions (CSMFs; §3.2) and velocity distribution functions (VDFs; §3.3) of neighbouring galaxies around our selected galaxy samples. The same methods are applied both to the observations from the SDSS (§2.1) and to seven mock catalogs generated from dark matter simulations (§2.2). The mock catalogs each include a different stellar mass–halo mass scatter from 0–0.6 dex for haloes $M_h < 10^{11}M_\odot$; to match observed constraints on scatter for higher-mass haloes, the input scatter is fixed at 0.2 dex for $M_h \gtrsim 10^{12}M_\odot$ and smoothly varied for $10^{11}M_\odot < M_h < 10^{12}M_\odot$ haloes (see Fig. 2 and §2.2). CSMFs and VDFs are calculated separately for low-mass galaxies (10^9 – $10^{10}M_\odot$) and high-mass galaxies (10^{10} – $10^{11}M_\odot$).

3.1 Isolation cuts

To constrain the scatter in the relationship between halo mass and stellar mass for central galaxies, we first apply

an isolation cut to galaxies in both simulations and observations to preferentially select central galaxies. As discussed in Appendix A, we take cuts to maximize completeness while retaining above 90% purity for the two galaxy mass ranges analyzed (Table 1). For the lower-mass sample (10^9 – $10^{10}M_\odot$), we select galaxies that are the most massive within 0.5 Mpc/h projected comoving distance r_p and a redshift distance Δv of $\pm 500 \text{ km s}^{-1}$ (5 Mpc h^{-1} in comoving line of sight distance). For the higher-mass sample (10^{10} – $10^{11}M_\odot$), we select galaxies that are the most massive within 1 Mpc h^{-1} projected comoving distance and a redshift distance of $\pm 1000 \text{ km s}^{-1}$ (10 Mpc h^{-1} in comoving line of sight distance). Using comoving distance instead of physical distance ensures a fairer comparison between the observations (at a range of redshifts) and simulated catalogs (at a single redshift)..

In the simulated galaxy catalogs, we use the distant observer approximation, so that projected distances are calculated along the X and Y axes, and redshift distances are calculated as $Z + \frac{v_Z}{H(z)}$, where v_Z is the Z -velocity and $H(z)$ is the Hubble expansion rate.

In the observations, we calculate the projected comoving distance as:

$$r_p = \theta_{\text{sep}} D(z_2) \quad (7)$$

where θ_{sep} is the angular distance between the two galaxies, and $D(z_2)$ is the comoving line-of-sight distance calculated from the redshift of the neighbouring galaxy. We use z_2 instead of the more common average of z_2 and z_1 (the redshift of the central galaxy) to minimize the difference between the volume searched around observed and simulated central galaxies due to the distant observer approximation.

3.2 Conditional stellar mass function

Here, we define the conditional stellar mass function (CSMF) as the number counts of neighbouring galaxies as a function of stellar mass within a cylindrical aperture and ± 1.5 Mpc/h redshift distance ($|\Delta v| < 150 \text{ km s}^{-1}$), averaged across all central galaxies. Neighbours are required to be galaxies within the same mass range as the sample (low-mass or high-mass) being considered. The observed CSMFs are calculated with the corrections for fibre collisions and maximum enclosed volume as described in §2.1.2.

For both low- and high-mass galaxies, we count neighbours within a projected distance cut of their central galaxy to maximize statistics and minimize any disagreements between the simulations and observations.

Average neighbour counts as a function of projected distance for low-mass and high-mass central galaxies (Figure 3) show consistency of observed to simulated catalogs, and reveal that satellite galaxies are concentrated at small radii. As expected, the low-mass galaxies are much more sensitive to the adopted scatter model. As motivated in Appendix B2, we take neighbours $50 < r_p < 200 \text{ kpc/h}$ for low-mass galaxies and neighbours $100 < r_p < 300 \text{ kpc/h}$ for high-mass galaxies for the highest consistency between simulated and observed catalogs and for the best statistics.

High values of scatter allow larger haloes to host smaller galaxies and smaller haloes to host larger galaxies, so the CSMFs of low-mass galaxies are expected to increase and

Scatter (dex)	Mass cut ($\log M_\odot$)	r_p cut (Mpc/h)	Δv cut (Mpc/h)	Purity	Completeness
0.0	9-10	0.5	5	0.987	0.533
0.6	9-10	0.5	5	0.953	0.513
0.0	10-11	1	10	0.982	0.433
0.6	10-11	1	10	0.912	0.407

Table 1. Purity and completeness of central galaxies for the chosen galaxy isolation cuts, as measured in our simulated galaxy catalogs.

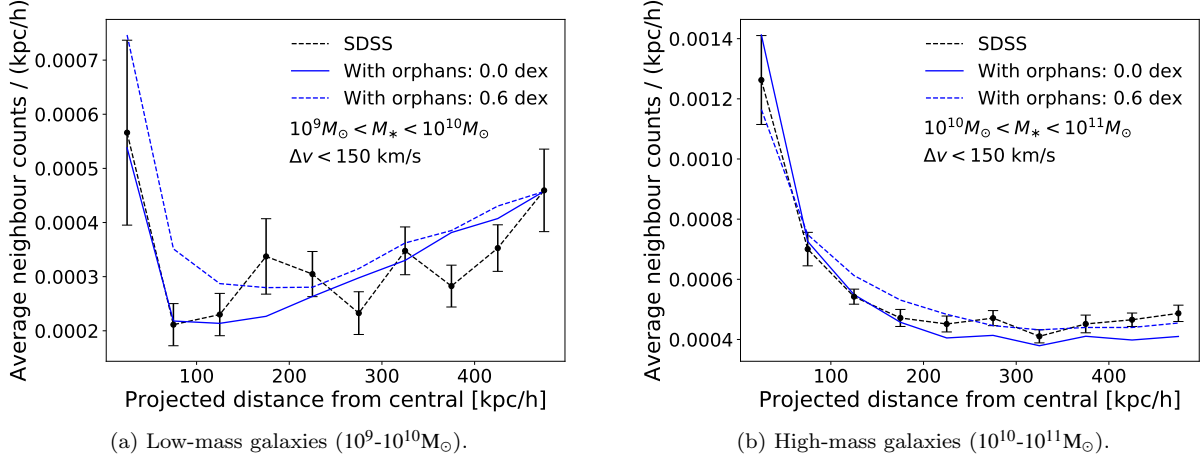


Figure 3. Average neighbour counts as a function of projected distance from low-mass and high-mass galaxies. Neighbours are galaxies in the same mass range within $\pm 1.5 \text{ Mpc h}^{-1}$ in redshift distance ($|\Delta v| < 150 \text{ km s}^{-1}$). The black line shows the observed distribution and the blue lines show the simulated distributions for different input scatters between stellar mass and halo mass.

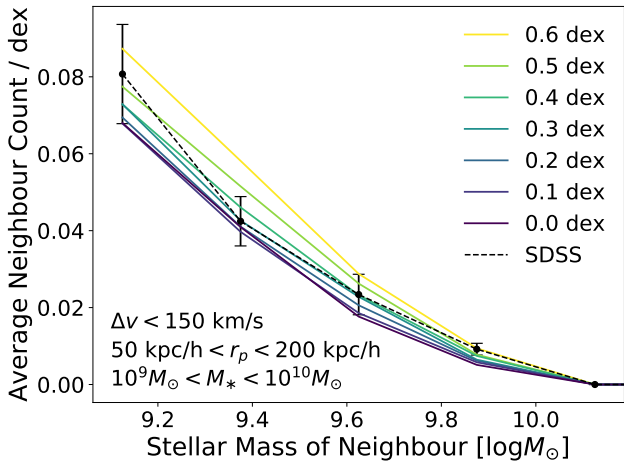


Figure 4. Comparison of observed and simulated conditional stellar mass functions for low-mass galaxies. Neighbours are galaxies in the same mass range and within 50-200 kpc/h projected and $\pm 1.5 \text{ Mpc h}^{-1}$ redshift distance ($|\Delta v| < 150 \text{ km s}^{-1}$).

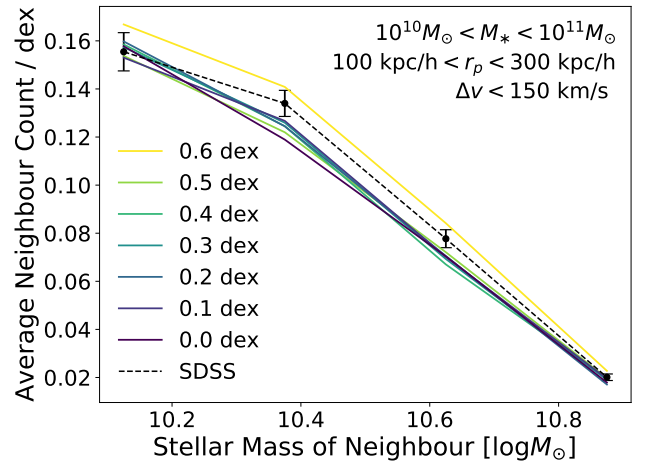


Figure 5. Comparison of observed and simulated conditional stellar mass functions for high-mass galaxies. Neighbours are galaxies in the same mass range and within 100-300 kpc/h projected and $\pm 1.5 \text{ Mpc h}^{-1}$ redshift distance ($|\Delta v| < 150 \text{ km s}^{-1}$).

the CSMFs of high-mass galaxies are expected to decrease. Nonetheless, because the magnitude of the scatter for high-mass haloes is fixed, the effect on the CSMF will be much larger for low-mass than for the high-mass galaxies. Low-mass galaxies clearly produce the expected trend (Figure 4), and high-mass galaxies (again as expected) show little distinction between scatters (Figure 5).

3.3 Velocity distribution

The velocity distribution function (VDF) gives the average number of neighbours as a function of redshift distance within a circular aperture. Again, we require neighbours to belong to the same mass range as the sample of central galaxies considered and take projected distance cuts of 50-200 kpc/h for low-mass galaxies and 100-300 kpc/h for

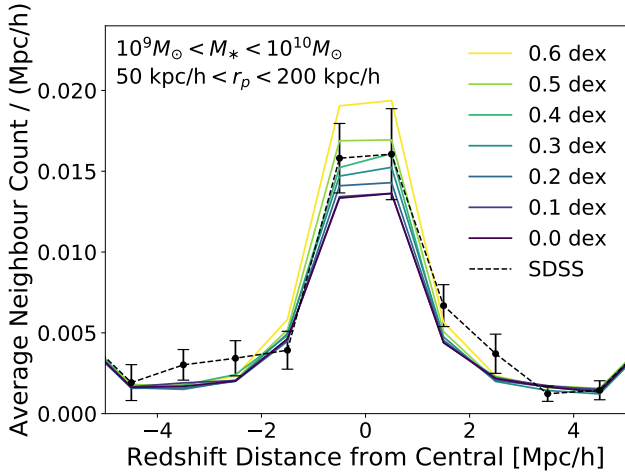


Figure 6. Comparison of observed and simulated velocity distribution functions for low-mass galaxies. Neighbours are galaxies in the same mass range and within 50-200 kpc/h projected distance. The upturn at large redshift distances is expected due to the isolation criterion (no larger galaxy within a redshift distance of 5 Mpc/h).

high-mass galaxies. Observed VDFs are calculated with the corrections described in §2.1.2.

Higher values of scatter allow larger haloes to host smaller galaxies and vice versa, and so, like the CSMFs, VDFs are expected to increase for low-mass central galaxies and decrease for high-mass central galaxies. We find the expected trend clearly differentiated for low-mass central galaxies (Figure 6) and again little distinction in high-mass central galaxies (Figure 7).

Given that our simulated catalogs have no difference for the scatter for high-mass ($\gtrsim 10^{12}M_{\odot}$) haloes, we expect (and find) that the greatest sensitivity to the input scatter comes from the CSMFs and VDFs for low-mass galaxies. Because the CSMFs and VDFs for high-mass galaxies are relatively insensitive to the input scatter, they instead serve as an important check that our adopted orphan model is realistic—i.e., that our satellite lifetimes are accurate.

4 RESULTS AND DISCUSSION

We compare the observed distributions to the simulations for varying values of scatter. No significant discrepancies exist between the models and the observations (Figures 4, 6, 5, and 7), giving confidence that the models are sufficiently flexible to describe the observations.

The CSMF and VDF for low-mass central galaxies are shown in Figures 4 and 6, respectively. They indicate that the observations are most consistent with low scatter (~ 0.2 dex). The high-mass CSMF and VDF (Figures 5 and 7) show less distinction across scatters, but are consistent with the simulated catalogs, suggesting that our orphan model is correctly capturing satellite lifetimes. Thus, we cannot put tight constraints on scatter without improved statistics beyond those available in the SDSS.

The methods we developed in §3 nonetheless produce distributions that are not only consistent with the observed

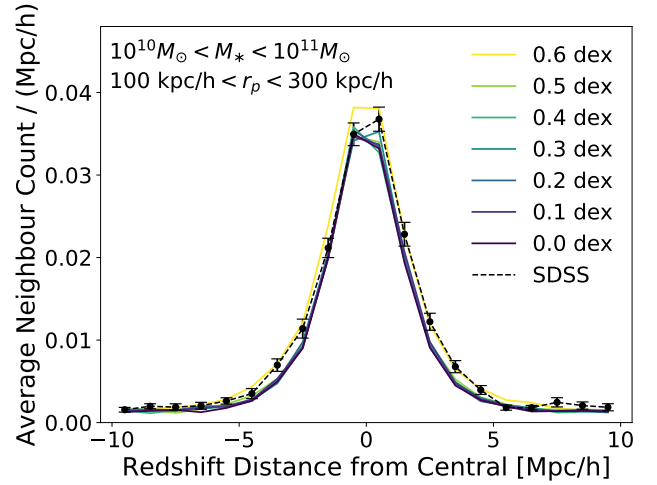


Figure 7. Comparison of observed and simulated velocity distribution functions for high-mass galaxies. Neighbours are galaxies in the same mass range and within 100-300 kpc/h projected distance.

Universe but also have the power to distinguish between different scatters for low-mass haloes. This method could be applied in the future to larger data sets; in particular, the upcoming Dark Energy Spectroscopic Instrument (DESI) Bright Galaxy Survey is anticipated to provide redshifts for over 10 million galaxies (DESI Collaboration et al. 2016) compared to the $\sim 200,000$ SDSS targets in our cut, and the pipeline will be able to distinguish close neighbor luminosity profiles with a higher degree of precision (Schlegel et al. 2015). Even regardless of the ability to probe satellites at closer projected distances, the resulting error bars would be better by at least a factor of $\sqrt{50}$, enabling very sensitive tests for both the orphan model adopted and for the scatter in the stellar mass–halo mass relation for galaxies with $M_h < 10^{11}M_{\odot}$. Based on the scatter-dependence of the low-mass CSMF (Figure 4), such reduced error bars could constrain scatter to approximately ± 0.05 dex and allow sensitive testing of satellite lifetimes and the orphan model described in §2.2.

5 CONCLUSIONS

We have developed a method (§3) to constrain scatter in the stellar mass–halo mass relation for central galaxies with host halo masses $M_h \leq 10^{11}M_{\odot}$ by comparing the mass and velocity distributions of neighbouring galaxies in dark matter simulations and observations. We find that the simulations produce very consistent results with the Sloan Digital Sky Survey, and comparison of the two suggests that low values of scatter (~ 0.2 dex) plausibly continue down to $M_h \sim 10^{11}M_{\odot}$. However, SDSS statistics are inadequate to firmly rule out larger values (§4). The method is nonetheless easily applied to future surveys, including the Dark Energy Spectroscopic Instrument experiment (DESI; DESI Collaboration et al. 2016), which will conclusively measure the stellar mass–halo mass scatter for low-mass haloes.

ACKNOWLEDGEMENTS

PB was partially supported through program number HST-HF2-51353.001-A, provided by NASA through a Hubble Fellowship grant from the Space Telescope Science Institute, which is operated by the Association of Universities for Research in Astronomy, Incorporated, under NASA contract NAS5-26555.

APPENDIX A: ISOLATION CUTS

Isolation cuts are applied to galaxies in both simulations at observations to select central galaxies. We choose cuts for low-mass (10^9 - $10^{10}M_{\odot}$) and high-mass (10^{10} - $10^{11}M_{\odot}$) galaxies to maximize purity and completeness, i.e., the ratio of simulated centrals matching our centrality cut to total centrality cut or total simulated centrals, respectively. We took cuts to maximize completeness while retaining above 90% purity for all values of scatter; both decrease monotonically with increasing scatter, but vary by less than 10% over 0.0-0.6 dex from typical values of $\sim 95\%$ purity and $\sim 50\%$ completeness (Table 1 in §3). As expected, purity rises and completeness falls with harsher isolation cuts for both low-mass and high-mass galaxies (Figures A1 and A2).

APPENDIX B: ORPHAN HALOES IN SIMULATIONS

Orphan satellite haloes are often included in simulations to match galaxy clustering, as described in §2.2. After generating catalogs with and without orphans, we find that models including orphan haloes provide a better match to observations.

B1 Inclusion of orphan haloes

Average neighbour counts as a function of projected distance from their central galaxy show agreement with the catalog including orphans, for both low- and high-mass galaxies (Figure B1). Errors on observations are calculated with the bootstrap resampling method described in §2.1.3. Clearly, catalogs generated without orphans grossly under-represent neighbours within 150 kpc/h, while catalogs with orphans place these neighbour counts within a sigma for high and low scatters.

B2 Motivating projected distance cuts

The characteristics of a galaxy’s nearest larger neighbour provide valuable information about clustering and serves as a measure of consistency between simulated and observed catalogs, motivating projected distance cuts on neighbours in the CSMFs and VDFs. The analysis below is carried out for catalogs adopting zero scatter, and the results are similar for 0.6 dex.

The mass distributions of nearest larger neighbours show close agreement between observations and both catalogs, for low- and high-mass galaxies (Figures B2 and B3).

Notable differences are seen in the distribution of projected distance to nearest larger neighbour for very near

(<100 kpc/h) neighbours, in the case of both low- and high-mass galaxies (Figures B4 and B5). Misleadingly, the high-mass distribution appears to more closely match catalogs without orphans.

This apparent deficit in near neighbours, particularly for high-mass galaxies, is likely due to observational incompleteness, i.e., overlapping luminosity profiles resulting in near neighbours going undetected. This effect would be more prominent in high-mass galaxies, since they have brighter luminosities. Inaccuracy in fiber collision corrections (described in §2.1.2) would also more greatly effect high-mass galaxies, which have higher degrees of spatial clustering. Galaxies this close may also be in the process of merging, which would further complicate disentangling them in the observational pipelines.

The distribution of velocity differences to nearest larger neighbours is shown in Figures B6 and B7; a normal distribution of noise centered on ± 30 km/s is added to the simulated velocity distributions to match uncertainties in redshift measurements. Observations are similar to both catalogs, but show slight differences from the catalog with orphans at very close (<50 km/s) redshift distances. Neighbours with small line-of-sight velocity differences may correspond to small projected distances as well, and then suffer the same issues of completeness as described above.

Overall, the differences in the distributions of nearest larger neighbour characteristics between observations and simulated catalogs (with or without orphan haloes) are small, and we use these results to motivate a projected distance cut of >50 kpc/h and >100 kpc/h for the low- and high-mass CSMFs and VDFs described in §3.2 and §3.3, respectively, and thus minimize these effects in our analysis.

REFERENCES

- Abazajian K. N., et al., 2009, *ApJS*, **182**, 543
Ade P. A., et al., 2016, *Astronomy & Astrophysics*, **594**, A13
Ahn C. P., et al., 2014, *ApJS*, **211**, 17
Behroozi P. S., Conroy C., Wechsler R. H., 2010, *ApJ*, **717**, 379
Behroozi P. S., Wechsler R. H., Wu H.-Y., 2013a, *ApJ*, **762**, 109
Behroozi P. S., Wechsler R. H., Wu H.-Y., Busha M. T., Klypin A. A., Primack J. R., 2013b, *ApJ*, **763**, 18
Behroozi P. S., Wechsler R. H., Conroy C., 2013c, *ApJ*, **770**, 57
Behroozi P. S., et al., 2015, *MNRAS*, **450**, 1546
Behroozi P., Wechsler R., Hearin A., Conroy C., 2018, preprint, ([arXiv:1806.07893](https://arxiv.org/abs/1806.07893))
Boylan-Kolchin M., Bullock J. S., Kaplinghat M., 2011, *MNRAS*, **415**, L40
Brinchmann J., Charlot S., White S. D. M., Tremonti C., Kauffmann G., Heckman T., Brinkmann J., 2004, *MNRAS*, **351**, 1151
Bryan G. L., Norman M. L., 1998, *ApJ*, **495**, 80
Chabrier G., 2003, *PASP*, **115**, 763
Conroy C., Wechsler R. H., Kravtsov A. V., 2006, *ApJ*, **647**, 201
DESI Collaboration et al., 2016, preprint, ([arXiv:1611.00036](https://arxiv.org/abs/1611.00036))
Elbert O. D., Bullock J. S., Garrison-Kimmel S., Rocha M., Oñorbe J., Peter A. H. G., 2015, *MNRAS*, **453**, 29
Garcia-Cely C., Chu X., 2017, preprint, ([arXiv:1705.06221](https://arxiv.org/abs/1705.06221))
Garrison-Kimmel S., Boylan-Kolchin M., Bullock J. S., Lee K., 2014, *MNRAS*, **438**, 2578
Garrison-Kimmel S., Bullock J. S., Boylan-Kolchin M., Bardwell E., 2017, *MNRAS*, **464**, 3108
Jiang F., van den Bosch F. C., 2016, *MNRAS*, **458**, 2848
Kauffmann G., et al., 2003, *MNRAS*, **346**, 1055

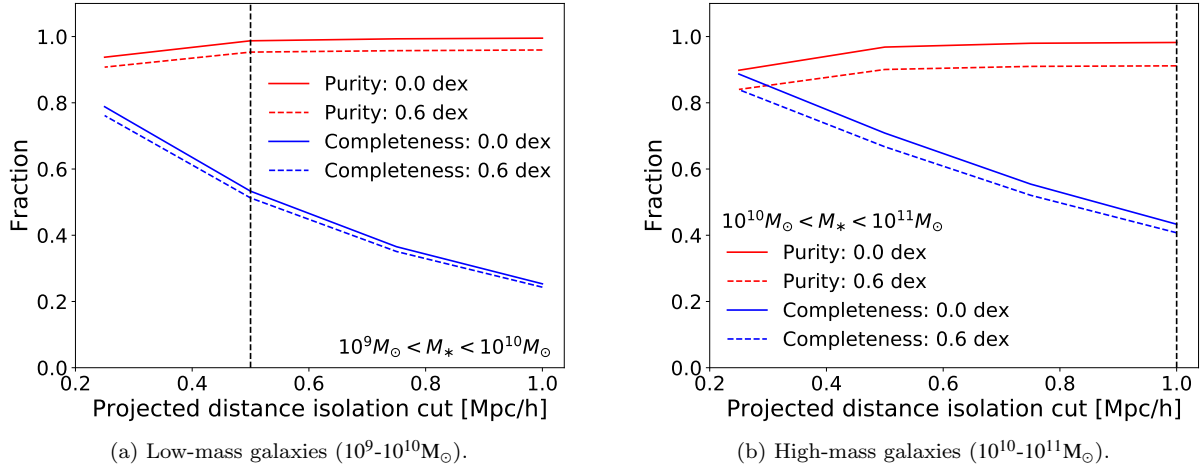


Figure A1. Purity and completeness for the central–satellite selection criteria for low-mass (left) and high-mass (right) simulated galaxies as a function of projected distance cut. Purity shown in red and completeness in blue (solid for 0.0 dex scatter, dashed for 0.6 dex scatter); the dashed vertical line indicates our chosen centrality cut.

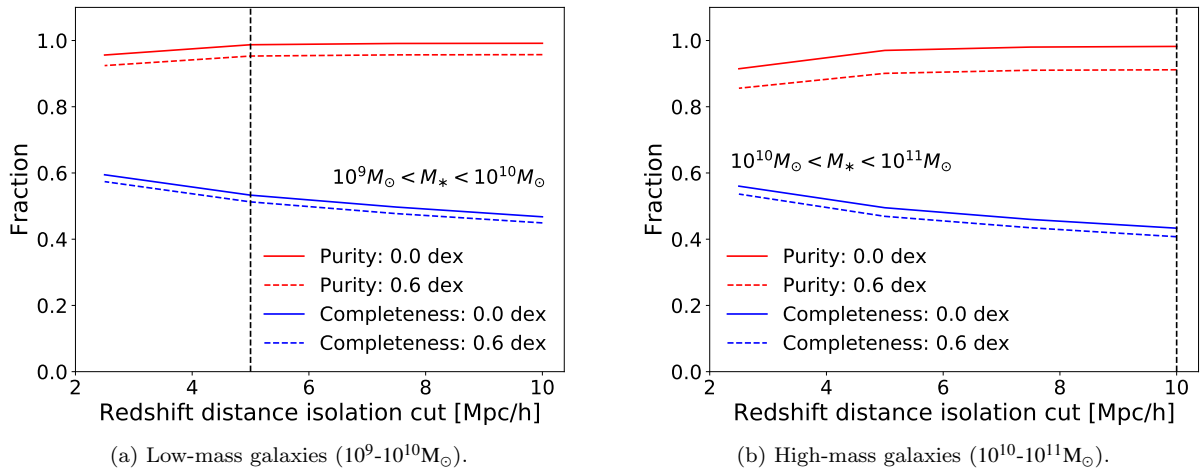


Figure A2. Purity and completeness for the central–satellite selection criteria for low-mass (left) and high-mass (right) simulated galaxies as a function of redshift distance cut. Purity shown in red and completeness in blue (solid for 0.0 dex scatter, dashed for 0.6 dex scatter); the dashed vertical line indicates our chosen centrality cut.

Kitzbichler M. G., White S. D. M., 2008, *MNRAS*, **391**, 1489
 Klypin A., Yepes G., Gottlöber S., Prada F., Heß S., 2016, *MNRAS*, **457**, 4340
 Kravtsov A. V., Klypin A. A., 1999, *ApJ*, **520**, 437
 Kravtsov A. V., Klypin A. A., Khokhlov A. M., 1997, *ApJS*, **111**, 73
 Kravtsov A. V., Vikhlinin A. A., Meshcheryakov A. V., 2018, *Astronomy Letters*, **44**, 8
 Marinoni C., Hudson M. J., 2002, *ApJ*, **569**, 101
 More S., van den Bosch F. C., Cacciato M., Mo H. J., Yang X., Li R., 2009, *MNRAS*, **392**, 801
 Moster B. P., Somerville R. S., Maulbetsch C., van den Bosch F. C., Macciò A. V., Naab T., Oser L., 2010, *ApJ*, **710**, 903
 Moster B. P., Naab T., White S. D. M., 2013, *MNRAS*, **428**, 3121
 Moster B. P., Naab T., White S. D. M., 2018, *MNRAS*, **477**, 1822
 Munshi F., Brooks A. M., Applebaum E., Weisz D. R., Governato F., Quinn T. R., 2017, preprint, ([arXiv:1705.06286](https://arxiv.org/abs/1705.06286))
 Nagai D., Kravtsov A. V., 2005, *ApJ*, **618**, 557
 Onions J., et al., 2012, *MNRAS*, **423**, 1200

Patton D. R., et al., 2002, *ApJ*, **565**, 208
 Patton D. R., Torrey P., Ellison S. L., Mendel J. T., Scudder J. M., 2013, *MNRAS*, **433**, L59
 Reddick R. M., Wechsler R. H., Tinker J. L., Behroozi P. S., 2013, *ApJ*, **771**, 30
 Rodríguez-Puebla A., Behroozi P., Primack J., Klypin A., Lee C., Hellinger D., 2016, *MNRAS*, **462**, 893
 Sawala T., et al., 2016, *MNRAS*, **456**, 85
 Schlegel D. J., et al., 2015, in American Astronomical Society Meeting Abstracts #225. p. 336.07
 Tinker J. L., Robertson B. E., Kravtsov A. V., Klypin A., Warren M. S., Yepes G., Gottlöber S., 2010, *ApJ*, **724**, 878
 Tinker J. L., et al., 2017, *ApJ*, **839**, 121

This paper has been typeset from a $\text{\TeX}/\text{\LaTeX}$ file prepared by the author.

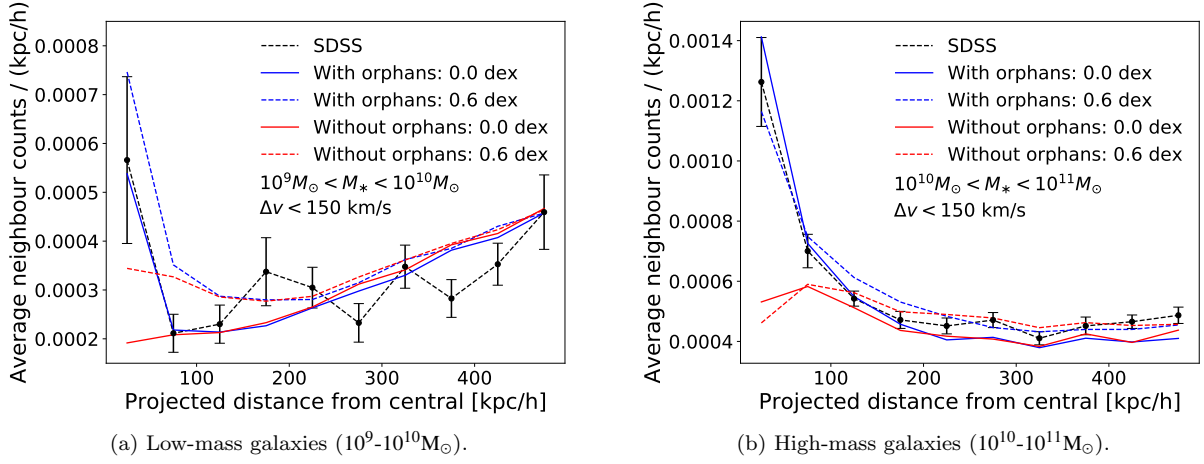


Figure B1. Average neighbour counts as a function of projected distance to low-mass (left) and high-mass (right) central galaxies, for catalogs generated with and without orphans. Neighbours are within ± 1.5 Mpc/h redshift distance. The black line shows the observed distribution, compared to the simulation with and without orphan haloes (blue and red lines, respectively) for different scatters.

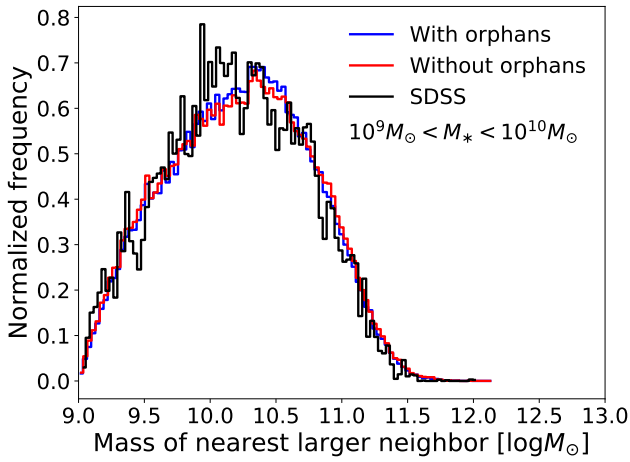


Figure B2. Normalized histogram of mass of nearest larger neighbour for high-mass galaxies (neighbours within 0.5 Mpc/h projected and ± 5 Mpc/h redshift distance). Compares observations (black), catalog with orphans for (blue), and catalog without orphans (red). Simulations are both for the model with zero scatter.

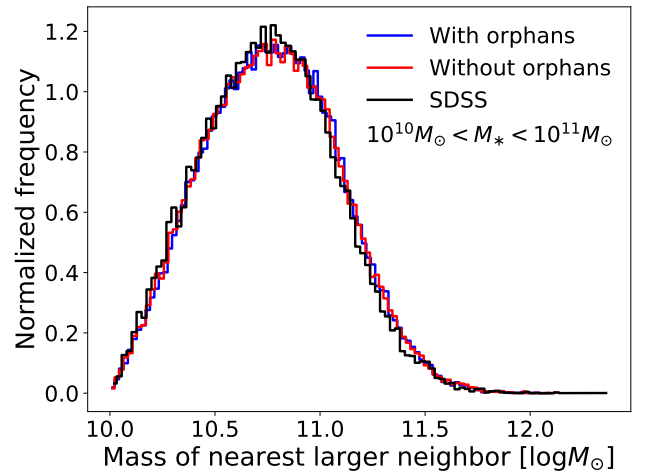


Figure B3. Normalized histogram of mass of nearest larger neighbour for high-mass galaxies (neighbours within 1 Mpc/h projected and ± 10 Mpc/h redshift distance). Compares observations (black), catalog with orphans for (blue), and catalog without orphans (red). Simulations are both for the model with zero scatter.

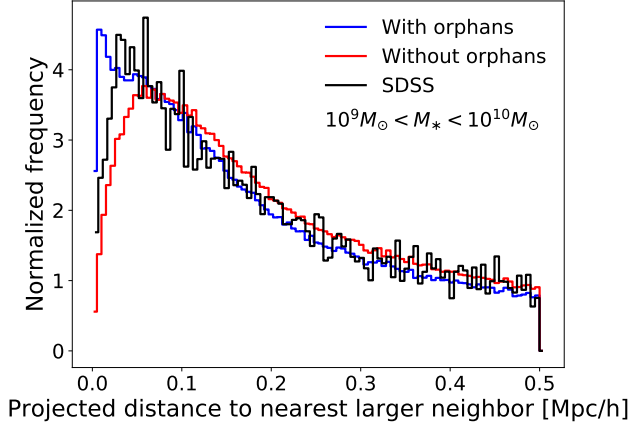


Figure B4. Normalized histogram of projected distance to nearest larger neighbour for high-mass galaxies (neighbours within 0.5 Mpc/h projected and ± 5 Mpc/h redshift distance). Compares observations (black), catalog with orphans for (blue), and catalog without orphans (red). Simulations are both for the model with zero scatter.

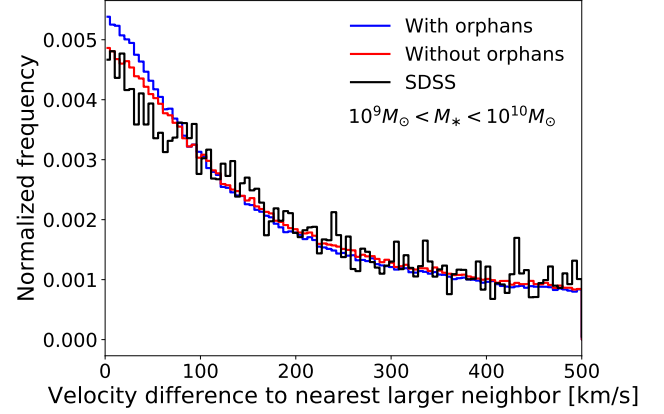


Figure B6. Normalized histogram of magnitude of velocity difference to nearest larger neighbour for high-mass galaxies (neighbours within 0.5 Mpc/h projected and ± 5 Mpc/h redshift distance). Compares observations (black), catalog with orphans for (blue), and catalog without orphans (red). Simulations are both for the model with zero scatter.

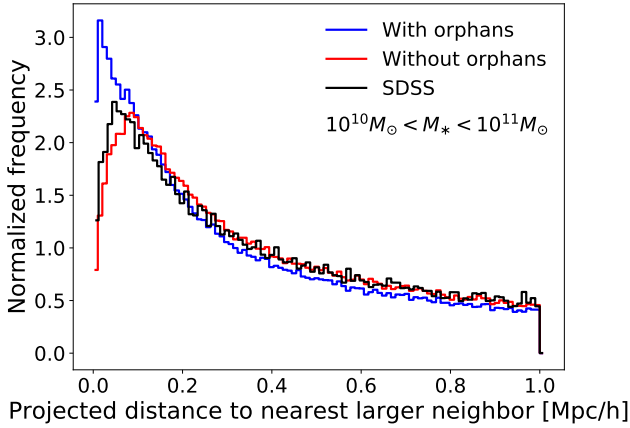


Figure B5. Normalized histogram of projected distance to nearest larger neighbour for high-mass galaxies (neighbours within 1 Mpc/h projected and ± 10 Mpc/h redshift distance). Compares observations (black), catalog with orphans for (blue), and catalog without orphans (red). Simulations are both for the model with zero scatter.

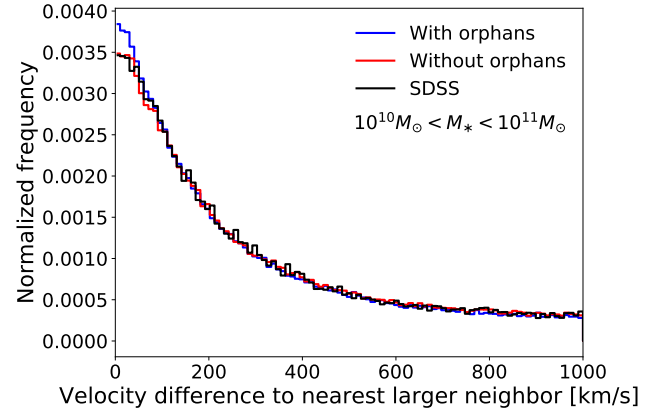


Figure B7. Normalized histogram of magnitude of velocity difference to nearest larger neighbour for high-mass galaxies (neighbours within 1 Mpc/h projected and ± 10 Mpc/h redshift distance). Compares observations (black), catalog with orphans for (blue), and catalog without orphans (red). Simulations are both for the model with zero scatter.